CHAPTER 2

THEORY AND LITERATURE REVIEWS

This chapter was review the introduction of battery, Thermodynamic Background, electrode processes, electrical double-layer capacity and ionic adsorption, mass transport to the electrode and electrochemical cells.

ELECTROCHEMICAL

Electrochemical devices can convert chemical energy into electrical energy by oxidation and reduction reactions, which occur at the electrodes. Electrochemical cell consists of an anode where oxidation takes place during discharge, cathode where reduction takes place and an electrolyte which conducts the electrons within the cell.

The maximum electric energy that can be delivered by the chemicals that are stored within or supplied to the electrodes in the cell depends on the change in free energy (ΔG) of the electrochemical couple.

It would be desirable if during the discharge all of this energy could be converted to useful electric energy. However, losses due to polarization occur when a load current i passes through the electrodes, accompanying the electrochemical reactions. These losses include: (1) activation polarization, which drives the electrochemical reaction at the electrode surface, and (2) concentration polarization, which arises from the concentration differences of the reactants and products at the electrode surface and in the bulk as a result of mass transfer.

These polarization effects consume part of the energy, which is given off as waste heat, and thus not all of the theoretically available energy stored in electrodes is fully converted in to useful electrical energy.

There is another important factor that strongly affects the performance or rate capability of a cell, the internal impedance of the cell. It causes a voltage drop during operation, which also consumes part of the useful energy as waste heat. The voltage drop due to internal impedance is usually referred to as ''Ohmic polarization'' or IR drop and is proportional to the current drawn from the system. The total internal impedance of a cell is the sum of the ionic resistance of the electrolyte (within the separator and the porous electrodes), the electronic resistances of the active mass, the current collectors and electrical tabs of both electrodes, and the contact resistance between the active mass and the current collector. These resistances are Ohmic in nature, and follow Ohm's law, with a linear relationship between current and voltage drop.

When connected to an external load R, the cell voltage E can be expressed as

$$E = E_0 - \left[\left(\eta_{ct} \right)_a + \left(\eta_c \right)_a \right] - \left[\left(\eta_{ct} \right)_c + \left(\eta_c \right)_c \right] - iR_i = iR \qquad (2.1)$$

where E_0 = electromotive force or open-circuit voltage of cell

$\left(\eta_{ct} \right)_a$, $\left(\eta_{ct} \right)_c$ = activation polarization or charge-transfer overvoltage at anode and cathode

$\left(\eta_c \right)_a$, $\left(\eta_c \right)_c$ = concentration polarization at anode and cathode

i = operating current of cell on load

R_i = internal resistance of cell

From equation number (2.1), the useful voltage delivered by the cell is reduced by polarization and the internal IR drop. It is only at very low operating currents, where polarization and the IR drop are small, that the cell may operate close to the open-circuit voltage and deliver most of the theoretically available energy. The relation between cell polarization and discharge current are shown in Figure 1.
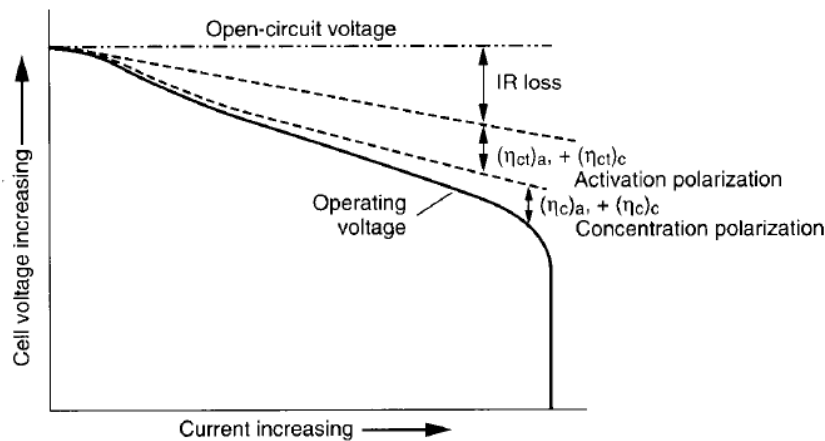
Figure 1 Cell polarizations as a function of operating current
(John Broadhead, Han C. Kuo, 1995)

Although the available energy of a battery or fuel cell depends on the basic electrochemical reactions at both electrodes, there are many factors which affect the magnitude of the charge-transfer reaction, diffusion rates, and magnitude of the energy loss. These factors include electrode formulation and design, electrolyte conductivity, and nature of the separators, among others. There exist some essential rules, based on the electrochemical principles, which are important in the design of batteries and fuel cells to achieve a high operating efficiency with minimal loss of energy.

1. The conductivity of the electrolyte should be high enough that the IR polarization is not excessively large for practical operation. The typical ranges of specific conductivities for various electrolyte systems used in batteries is seem in Table 1. Batteries are usually designed for specific drain rate applications, ranging from µA to several 100 A. For a given electrolyte, a cell may be designed to have improved rate capability, with a higher electrode interfacial area and thin separator, to reduce the IR drop due to electrolyte resistance. Cells with a spirally wound electrode design are typical examples.

2. Electrolyte salt and solvents should have chemical stability to avoid direct chemical reaction with the anode or cathode materials.

Table 1 Conductivity ranges of various electrolytes at ambient temperature

Electrolyte system	Specific conductivity, $\Omega^{-1}cm^{-1}$
Aqueous electrolytes	$1-5\times10^{-1}$
Molten salt	$\sim 10^{-1}$
Inorganic electrolytes	$2\times10^{-2}-10^{-1}$
Organic electrolytes	$10^{-3}-10^{-2}$
Polymer electrolytes	$10^{-7}-10^{-2}$
Inorganic solid electrolytes	$10^{-8}-10^{-5}$

(John Broadhead, Han C. Kuo, 1995)

3. The rate of electrode reaction at both the anode and the cathode should be sufficiently fast so that the activation or charge-transfer polarization is not too high to make the cell inoperable. A common method of minimizing the charge-transfer polarization is to use a porous electrode design. The porous electrode structure provides a high electrode surface area within a given geometric dimension of the electrode and reduces the local current density for a given total operating current.

4. In most battery and fuel cell systems, part or all of the reactants are supplied from the electrode phase and part or all of the reaction products must diffuse or be transported away from the electrode surface. The cell should have adequate electrolyte transport to facilitate the mass transfer to avoid building up excessive concentration polarization. Proper porosity and pore size of the electrode, adequate thickness and structure of the separate or, and sufficient concentration of the reactants in the electrolyte are very important to ensure functionality of the cell. Mass-transfer limitations should be avoided for normal operation of the cell.

5. The material of the current collector or substrate should be compatible with the electrode material and the electrolyte without causing corrosion problems. The design of the current collector should provide a uniform current distribution and low contact resistance to minimize electrode polarization during operation.

6. For rechargeable cells it is preferable to have the reaction products remain at the electrode surface to facilitate the reversible reactions during charge and discharge. The reaction products should be stable mechanically as well as chemically with the electrolyte.

In general, the principles and various electrochemical techniques described in this chapter can be used to study all the important electrochemical aspects of a battery or fuel cell. These include the rate of electrode reaction, the existence of intermediate reaction steps, the stability of the electrolyte, the current collector, the electrode materials, the mass-transfer conditions, the value of the limiting current, the formation of resistive films on the electrode surface, the impedance characteristics of the electrode or cell, and the existence of the rate-limiting species.

In a cell, reactions essentially take place at two areas or sites in the device. These reaction sites are the electrode interfaces. In generalized terms, the reaction at one electrode (reduction in forward direction) can be represented by

$$aA + ne \rightleftharpoons cC \tag{2.2}$$

where a molecules of A take up n electrons e to form c molecules of C. At the other electrode, the reaction (oxidation in forward direction) can be represented by

$$bB - ne \rightleftharpoons dD \tag{2.3}$$

The overall reaction in the cell is given by addition of these two half-cell reactions

$$aA + bB \rightleftharpoons cC + dD \tag{2.4}$$

The change in the standard free energy ΔG^0 of this reaction is expressed as

$$\Delta G^0 = -nFE^0 \tag{2.5}$$

Where F = constant known as the Faraday (96,487 coulombs)

               E^0 = standard electromotive force

When conditions are other than in the standard state, the voltage E of a cell is given by the Nernst's equation,

$$E = E^0 - \frac{RT}{nF} \ln \frac{a_C^c a_D^d}{a_A^a a_B^b} \tag{2.6}$$

where $a_{a,b,c,d}$ = activity of relevant species

          R = gas constant

          T = absolute temperature

The change in the standard free energy ΔG^0 of a cell reaction is the driving force which enables a battery to deliver electrical energy to an external circuit. The measurement of the electromotive force, incidentally, also makes available data on changes in free energy, entropies and enthalpies together with activity coefficients, equilibrium constants, and solubility products.

Direct measurement of single (absolute) electrode potentials is considered practically impossible. To establish a scale of half-cell or standard potentials, a reference potential ''zero'' must be established against which single electrode potentials can be measured. By convention, the standard potential of the H_2 / H^+ (aq) reaction is taken as zero and all standard potentials are referred to this potential. Table 2 list the standard potentials of a number of anode and cathode materials.

Table 2 Standard potentials of electrode reactions at 25 °C

Electrode reaction	E°, V	Electrode reaction	E°, V
$Li^{+}+e \rightleftharpoons Li$	-3.01	$Ti^{+}+e \rightleftharpoons Ti$	-0.34
$Rb^{+}+e \rightleftharpoons Rb$	-2.98	$Co^{2+}+2e \rightleftharpoons Co$	-0.27
$Cs^{+}+e \rightleftharpoons Cs$	-2.92	$Ni^{2+}+2e \rightleftharpoons Ni$	0.23
$K^{+}+e \rightleftharpoons K$	-2.92	$Sn^{2+}+2e \rightleftharpoons Sn$	-0.14
$Ba^{2+}+2e \rightleftharpoons Ba$	-2.92	$Pb^{2+}+2e \rightleftharpoons Pb$	-0.13
$Sr^{2+}+2e \rightleftharpoons Sr$	-2.89	$D^{+}+e \rightleftharpoons 1/2D_2$	-0.003
$Ca^{2+}+2e \rightleftharpoons Ca$	-2.84	$H^{2+}+e \rightleftharpoons 1/2H_2$	0.000
$Na^{+}+e \rightleftharpoons Na$	-2.71	$Cu^{2+}+2e \rightleftharpoons Cu$	0.34
$Mg^{2+}+2e \rightleftharpoons Mg$	-2.38	$1/2O_2+H_2O+2e \rightleftharpoons 2OH$	0.40
$Ti^{+}+2e \rightleftharpoons Ti$	-1.75	$Cu^{+}+2e \rightleftharpoons Cu$	0.52
$Be^{2+}+2e \rightleftharpoons Be$	-1.70	$Hg^{2+}+2e \rightleftharpoons 2Hg$	0.80
$Al^{3+}+3e \rightleftharpoons Al$	-1.66	$Ag^{+}+e \rightleftharpoons Ag$	0.80
$Mn^{2+}+2e \rightleftharpoons Mn$	-1.05	$Pd^{2+}+2e \rightleftharpoons Pd$	0.83
$Zn^{2+}+2e \rightleftharpoons Zn$	-0.76	$Ir^{3+}+3e \rightleftharpoons Ir$	1.00
$Ga^{3+}+3e \rightleftharpoons Ga$	-0.52	$Br_2+2e \rightleftharpoons 2Br$	1.07
$Fe^{2+}+2e \rightleftharpoons Fe$	-0.44	$O_2+4H^{+}+4e \rightleftharpoons 2H_2O$	1.23
$Cd^{2+}+2e \rightleftharpoons Cd$	-0.40	$Cl_2+ke \rightleftharpoons 2Cl$	1.36
$In^{3+}+3e \rightleftharpoons In$	-0.34	$F_2+2e \rightleftharpoons In$	2.87

(John Broadhead, Han C. Kuo, 1995)

The operation of a cell during discharge is also shown schematically in Figure 2 When the cell is connected to an external load, electrons flow from the anode, which is oxidized, through the external load to the cathode, where the electrons are accepted and the cathode material is reduced. The electric circuit is completed in the electrolyte by the flow of anions (negative ions) and cations (positive ions) to the anode and cathode, respectively.
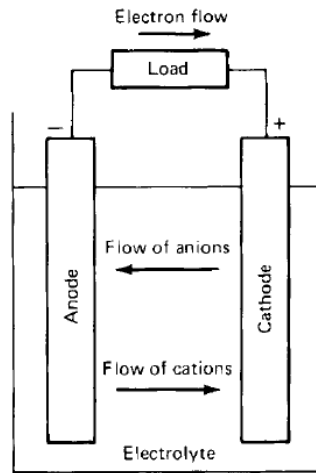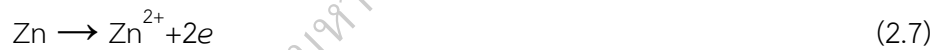
Figure 2 Electrochemical operation of a cell (discharge)
(David Linden, 1995)

The discharge reaction can be written, assuming a metal as the anode material and a cathode material such as chlorine (Cl_2), as follows:

Negative electrode: anodic reaction (oxidation, loss of electrons)

$$Zn \longrightarrow Zn^{2+} + 2e \tag{2.7}$$

Positive electrode: cathodic reaction (reduction, gain of electrons)

$$Cl_2 + 2e \longrightarrow 2Cl^- \tag{2.8}$$

Overall reaction (discharge):

$$Zn + Cl \longrightarrow Zn^{2+} + 2Cl^- (ZnCl_2) \tag{2.9}$$

During the recharge of a rechargeable or storage cell, the current flow is reversed and oxidation takes place at the positive electrode and reduction at the negative electrode, as shown in Figure 2 As the anode is, by definition, the electrode at which oxidation occurs and the cathode the one where reduction takes place, the positive electrode is now the anode and the negative the cathode. In the example of the Zn/Cl_2 cell, the reaction on charge can be written as follows: Negative electrode: cathodic reaction (reduction, gain of electrons)

$$Zn^{2+} + 2e \longrightarrow Zn \qquad (2.10)$$

Positive electrode: anodic reaction (oxidation, loss of electrons)

$$2Cl^- \longrightarrow Cl_2 + 2e \qquad (2.11)$$
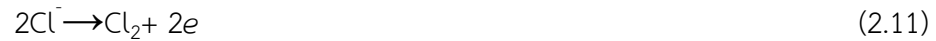
Overall reaction (charge):

$$Zn^{2+} + 2Cl^- \longrightarrow Zn + Cl_2 \qquad (2.12)$$

LITERATURE REVIEWS

In 2013, M. Blanco et al., the electrochemical behavior of Cu–16 (wt.%) Zn–6.5 (wt.%) Al alloy containing the β'-phase(martensite) is studies in borate buffer solution (pH 8.4) by means of open-circuit potential (E_{OC}), electrochemical impedance spectroscopy (EIS) and cyclic voltammetry (CV). The alloy E_{OC} was –0.29 Vvs. Hg/HgO/OH⁻, similar to that of pure copper in this medium, indicating that the processes which occur on the alloy surface are mainly governed by copper. EIS response was related to the dielectricand transmission properties of the complex oxide layer. The CVs showed peaks concerning the redoxreactions for copper and zinc. These peaks were assigned to the formation and reduction of copper andzinc species. Furthermore, they showed that the copper oxidation is suppressed by the presence of zinc and aluminum in the alloy composition. The copper and zinc oxidation to form complex oxide layers and the reduction of the different metallic oxides generated in the anodic potential scan suggest that a solid state reaction could determine the metallic oxide formation.
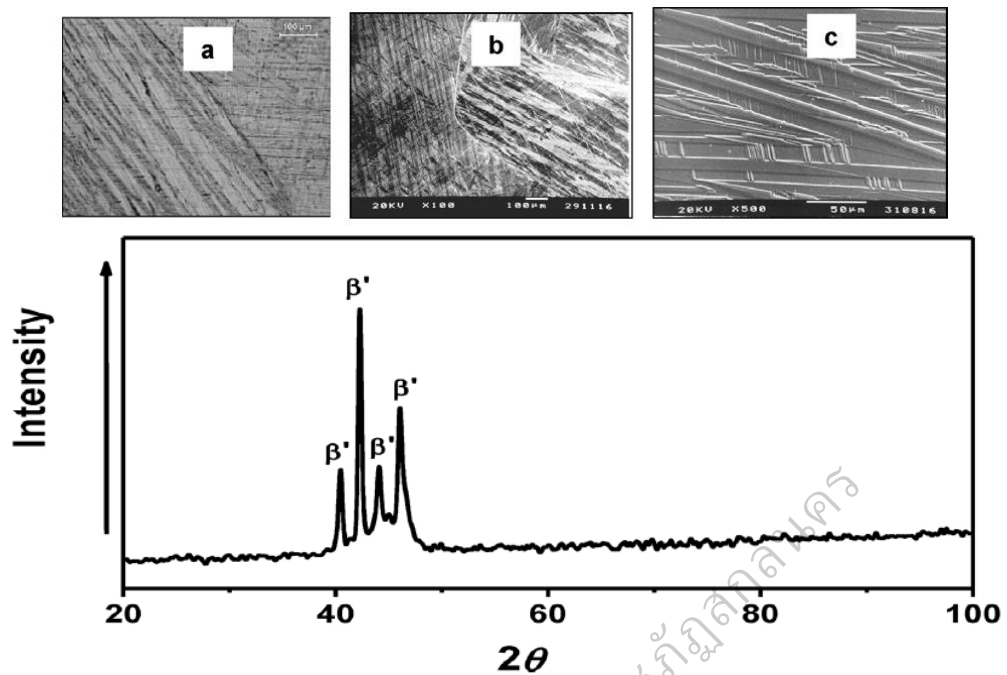
Figure 3 Optical microscopy (a) and SEM (b-c) images of Cu–16%Zn–6.5%Al alloy after annealing at 850 °C for 3 h and quenched at 100 °C and subsequently at 0 °C into water. Alloy structure revealed after etching with an alcoholic ferric chloride solution. XRD pattern of quenched Cu–16%Zn–6.5%Al alloy evidencing the martensitic structure
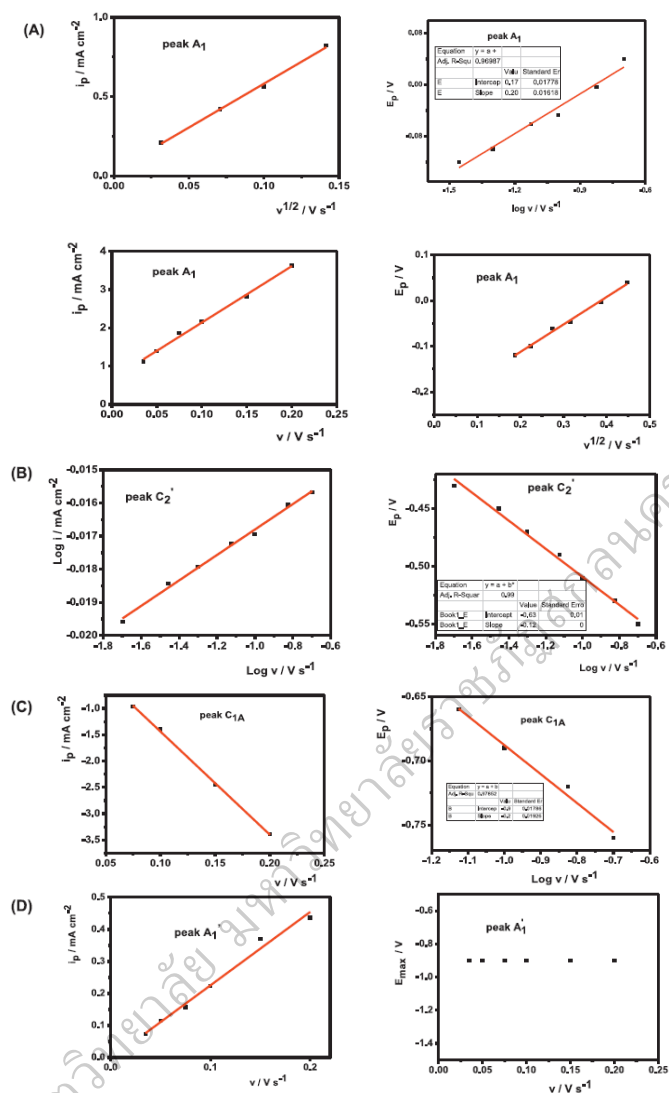
(M. Blanco, 2013)

Figure 4 Peak current densities versus scan rate and peak potentials versus scan
rate
(M. Blanco, 2013)

In 2014, Fengxia Wu et al., A zinc-aluminum layered double hydroxides
(Zn-Al LDHs) film was prepared on AZ91D magnesium (Mg) alloy substrate by
electrochemical deposition method. The characteristics of the film were
investigated by X-ray diffraction (XRD), Fourier transform infrared (FT-IR) and
scanning electronic microscope (SEM). The electrodeposited film is composed of
crystalline Zn-Al LDHs with nitrate inter-calation. The Zn-Al LDHs film is uniform
and dense though there also presented some small flaws andcracks. The cross

cut tape test showed that the film adhered well to the substrate. Polarization and EIS measurements revealed that the LDHs coated Mg alloy had better corrosion resistance compared to that of an uncoated in 3.5 wt.% NaCl solution, indicating that the Zn-Al LDHs film could effectively protect Mg alloy from corrosion.
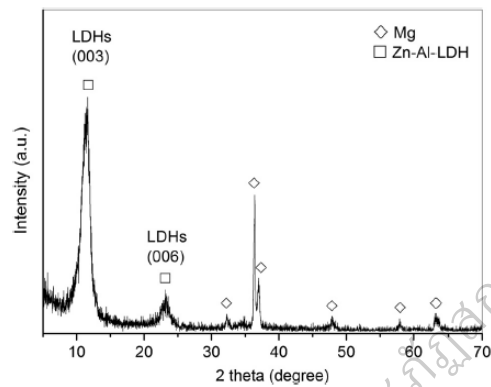
Figure 5 XRD pattern of the AZ91D magnesium alloy treated in the
Zn^{2+}/Al^{3+} solutionat applied potential of −1.7 V
(Fengxia Wu, 2014)
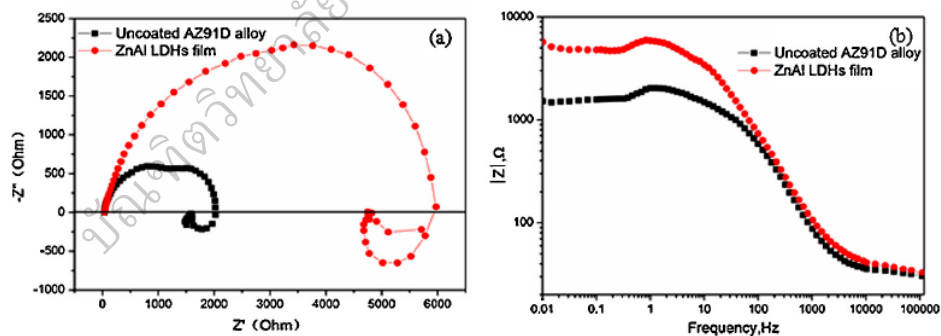
Figure 6 Nyquist plots of the electrochemical impedance response (a), and Bode
plots of |Z|vs. frequency (b) an uncoated and Zn-Al LDHs coated AZ91D
alloy in 3.5 wt.% NaCl solution
(Fengxia Wu, 2014)

In 2014, Mikel Pino et al., developed new materials for Al/air batteries, the evaluation and characterization of commercial aluminum alloys, namely, Al2000, Al2000Clad and Al7000,as anodes in alkaline electrolyte batteries has

been performed (see as Figure 7).Their self-corrosion rate, hydrogen evolution rate and electrochemical properties, including open circuit potentials, polarization characteristics and potentiodynamic measurements, were examined in a 4 mol KOH solution display as Table 3 Among the tested alloys, Al2000 was found to be the most promising because it exhibits a high open circuit potential, a good anode efficiency and a minimum corrosion rate. Al2000/NiOOH and Al2000/air batteries were tested. Electrolyte concentrations between 0.01 and 4 mol KOH were studied, and discharge currents between 0.8 and 20 mA cm^{-2} were imposed to analyze the evolution of the E_{cell}. Conversely, the Al7000 alloy exhibited the highest corrosion rate and H_2 evolution compared to the other alloy.
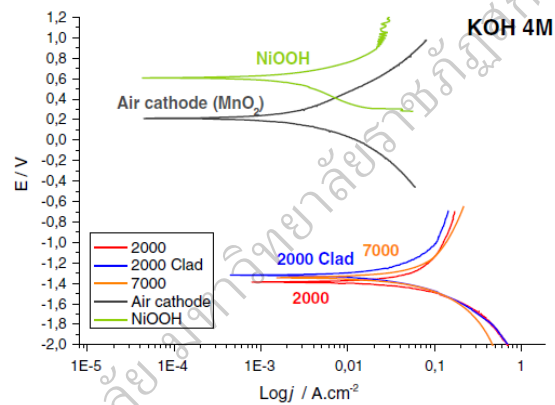
Figure 7 Polarization curves at a scan rate of v = 1 mV s^{-1} and 25 °C in a 4 mol KOH solution for Al2000 Clad, Al2000 and Al7000 anodes and NiOOH and air cathodes

(Mikel Pino, 2014)

Table 3 Stabilization potential values, Eplateau, of the Al alloys from the
potentiodynamic study in 4 mol KOH

4 mol KOH			
	Al2000	Al7000	Al2000Clad
	$E_{plateau}$/V	$E_{plateau}$/V	$E_{plateau}$/V
20 mA cm^{-2}	-1,334	-1.329	-1.328
40 mA cm^{-2}	-1.246	-1.292	-1.198
60 mA cm^{-2}	-1.200	-1.276	-1.117
80 mA cm^{-2}	-1.132	-1.203	-1.058
100 mA cm^{-2}	-	-	-0.997

(Mikel Pino, 2014)

In 2014, Vincenzo Caramiaet et al., reported batteries for electric drive
vehicles in the near future, the so-called metal–air batteries could replace the
ion-based technology as shown in Figure 8. Mathematical modeling of electrically
is rechargeable Zn–air batteries. It has appeared on the mathematical modeling
of the anode thickness and the optimal KOH concentration. A single-cell
rechargeable Zn–air batteries are able to estimate the I–V response of the cell,
the individual Zn and O_2 electrode potentials as well as the potential and
concentration profiles as shown in Figure 9. The model proposed in consists of
two partial differential equations for the material balance of ions moving in the
electrolyte and solid species locked in the anode.
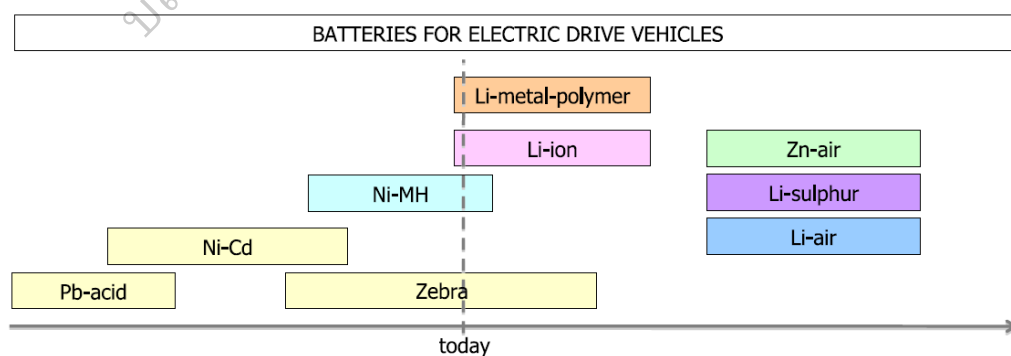
Figure 8 Batteries for electric drive vehicles
(Vincenzo Caramiaet, 2014)
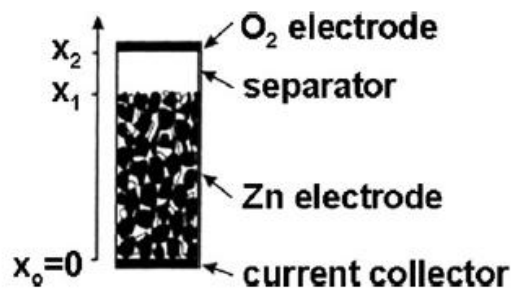
Figure 9 Model of the one-dimension single-cell Zn–air battery
(Vincenzo Caramiaet, 2014)

In 2015, Caizhen Yao et al., prepared and characterized Zn–Al–Mg cast alloys with different Mg contents. The solidification process of melt liquids and the formation mechanism of intermetallic are analyzed. The influence of microstructure on corrosion resistance property of alloy is also investigated. The microhardness of Zn–Al–Mg alloys increased with increasing of Mg content, which is due to the grain refining effect. Ternary eutectic structures (Zn/Al/Zn–Mg intermetallic) are found in Zn–Al–Mg alloys. Polarization analyse reveals that Zn– 5 wt.% Al–2 wt.% Mg (ZA5M2) alloy has the lowest corrosion current density of 1.03×10^{-3} A/cm^2 among all tested samples. Electrochemical impedance spectroscopy indicates that with the increasing of Mg content, the resistance of corrosion product increases from about 930 Ω of Zn–5 wt.% Al alloy to 8360 Ω of ZA5M2 alloy. The formation of nanostructured eutectic Zn/Al/Mg$_2$Zn$_{11}$ is probably the key factor of the improved corrosion property.
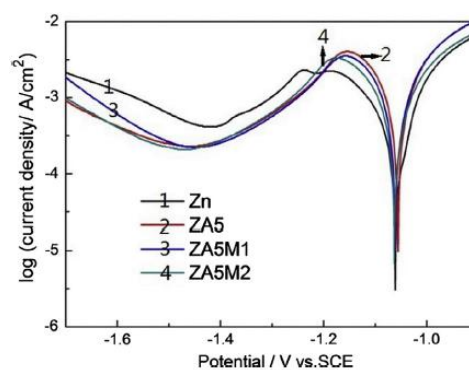
Figure 10 Potentio-dynamic polarization curves of prepared specimens
(Caizhen Yao, 2015)
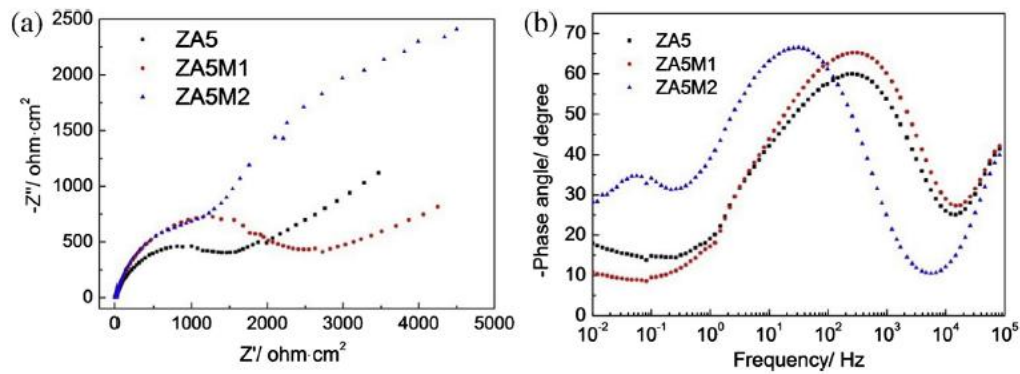
Figure 11 EIS spectra for prepared Zn–Al–Mg alloys in 3.5 wt.% NaCl solution:
(a) Nyquist diagrams; (b) Bode phase diagrams
(Caizhen Yao, 2015)

In 2015, Kun ZHOU et al. investigating the corrosion and electrochemical behaviors of 7A09 Al–Zn–Mg–Cu alloy in 3.5% NaCl (mass fraction) solution using complementary techniques such as scanning electron microscopy (SEM), metallographic microscopy and electrochemical measurements. The results show that both pitting corrosion from or around the intermetallic particles and intergranular corrosion are observed after the immersion test due to the in homogeneous nature of the microstructure of the 7A09 alloy. The preferential dissolution of the anodic Cu-depleted zone along grain boundaries is believed to be the possible cause of intergranular corrosion. The passivation and depassivation of this alloy show significant dependence of immersion time, owing to the formation and dissolution of various passive films on the sample surfaces. Furthermore, the corrosion process and corrosion mechanism are also analyzed.
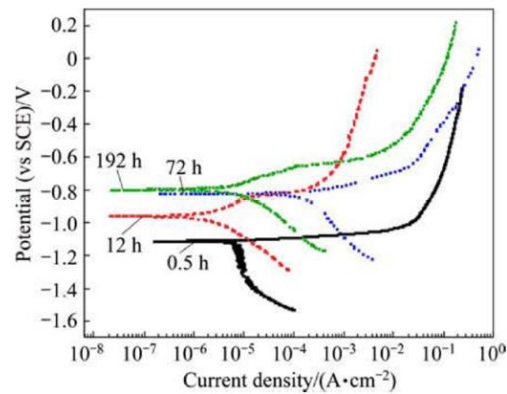
Figure 12 Potentiodynamic polarization curves of 7A09-T6 alloyimmersed in 3.5%
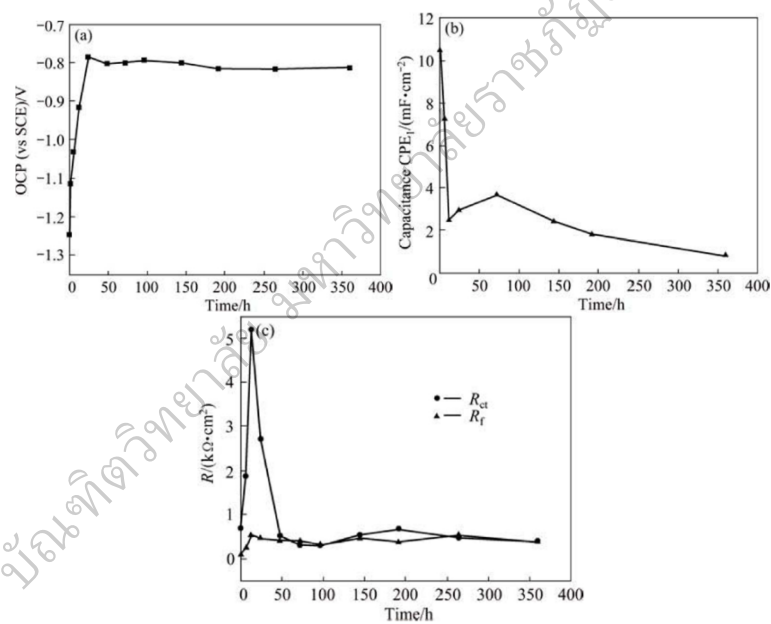NaCl solution as function of immersion time
(Kun ZHOU, 2015)

Figure 13 Evolution of electrochemical parameters: (a) Open circuit potential
(OCP); (b) Low frequency capacitance; (c) Rctand Rf values for 7A09-T6 alloy
samples in 3.5% NaCl solutionas function of immersion time
(Kun ZHOU, 2015)

In 2016, Gh. Barati Darband et al. reported electrophosphating is the
novel method for accelerating the low temperature phosphating bath. This
method can be performed as cathodic and anodic treatments. Both of them

influence the coating deposition mechanism and therefore coating properties. In this study Zn–Ni electrophosphate coating is applied on galvanized steel using cathodic and anodic electrochemical methods. Microstructure, composition and corrosion resistance of coatingwere characterized by using a scanning electron microscopy, X-ray diffraction method and potentiodynamic polarization test respectively. The results of this study indicated that, by using cathodic method, compact phosphatecoating with high corrosion resistance can be obtained. The result of X-ray diffraction pattern indicated the presence of Zn and Ni along with zinc and nickel phosphate in the phosphate layer. It is indicated that the phosphatecrystal shape of cathodically coating was flower and plate like and only flower like crystals are formed in anodicallycoating. Also results indicated that, the phosphate coating obtained by anodic electrochemical method hashigh porosity and consequently poor corrosion resistance. Also, based on the study results, applications proposedfor coatings that obtained by cathodic and anodic electrochemical methods.
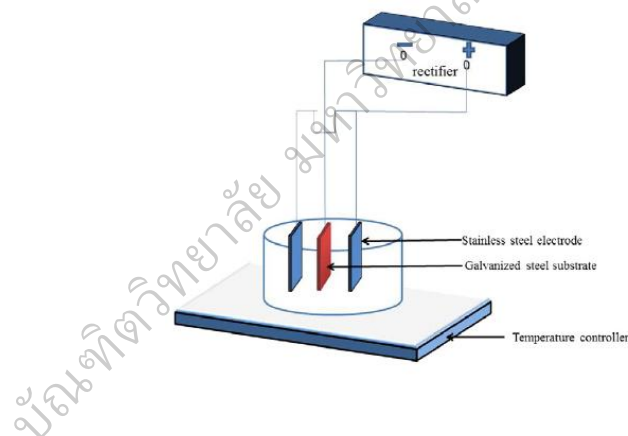
Figure 14 Schematic of the setup used for electrophosphating treatment
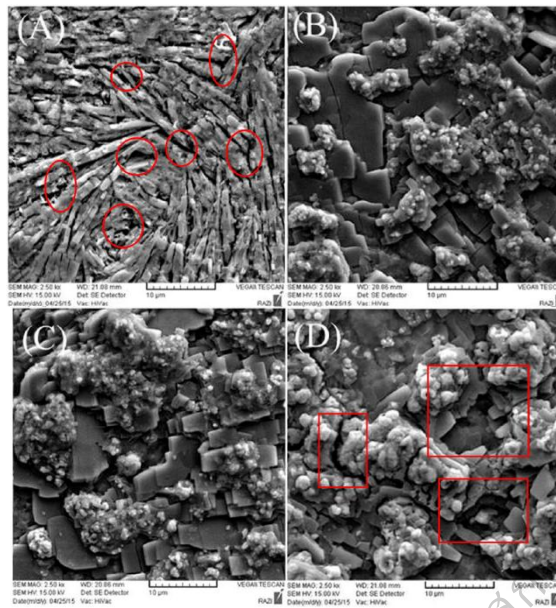(Gh. Barati Darband, 2016)

Figure 15 SEM micrograph of Zn–Ni electrophosphate coating obtained by the cathodic electrochemical method at different current densities A) 5, B) 15, C) 25, D) 35 mA/cm^2

(Gh. Barati Darband, 2016)

In 2016, Li Wen et al. reported Mg-Al-Pb-Zn alloy is a typical anode material used for high-power seawater activated battery. Thechemical composition of a series of Mg-Al-Pb-(Zn) alloys is optimized by a L$_9$ orthogonal array test andthe effects of alloying elements, such as aluminium, lead and zinc, on electrochemical properties are investigated through signal-to-noise ratio (S/N) analysis. Microstructure characterization and half-celltest demonstrate that the selected optimal Mg-6%Al-7%Pb-0.5%Zn (wt%) alloy is a good candidate as an anode material for seawater activated battery application due to its high discharge activity, negativedischarge potential in large current densities and comparatively higher anode utilization efficiency. The prototype battery assembled with Mg-6%Al-7%Pb-0.5%Zn alloy as anode and AgCl as cathode revealsexcellent discharge performance, reaching a superior specific energy of 155 Wh•kg^{-1}
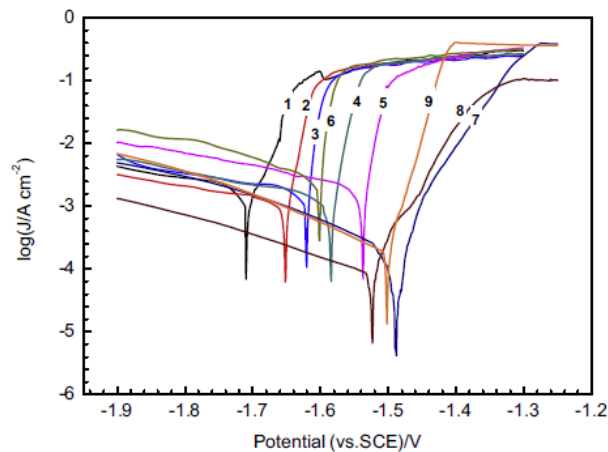
Figure 16 Potentiodynamic polarization behavior of No.1 ~ No.9 experimental
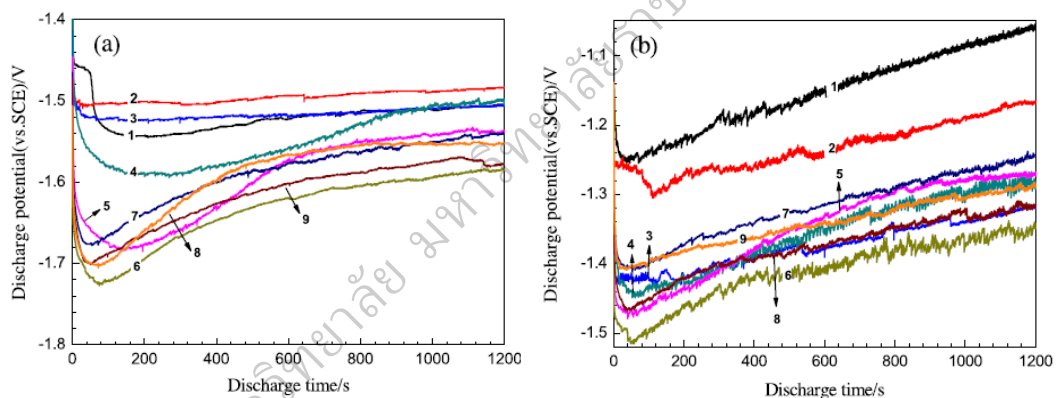alloys
(Li Wen, 2016)

Figure 17 Galvanostatic discharge behavior of No.1~ No.9 experimental alloys.
(a) Galvanostatic discharge behavior at 150 mA•cm^{-2}, (b) galvanostatic
discharge behavior at 350 mA•cm^{-2}
(Li Wen, 2016)

In 2016, Naiguang Wang et al. reported the discharge and corrosion
behaviour of Mg-Li-Al-Ce-Y-Zn alloy in 3.5 wt.% NaCl solution is investigated by
electrochemical techniques, and compared with that of pure magnesium, AZ31,
and Mg-Li-Al-Ce-Yalloys. The results indicate that Mg-Li-Al-Ce-Y-Zn exhibits
desirable performance in half-cell tests and battery discharge. The peak power
density of the Mg-air battery with Mg-Li-Al-Ce-Y-Zn anode is comparable with that

of Mg-H$_2$O$_2$ semi-fuel battery. Its anodic efficiency at 10 mA•cm^{-2} reaches (60.6 ± 0.2)%, which is significantly higher than that of the state-of-the-art AP65 magnesium alloy. Moreover, the dissolution mechanism of Mg-Li-Al-Ce-Y-Zn is also characterized based on electrochemical response and microstructure observation.
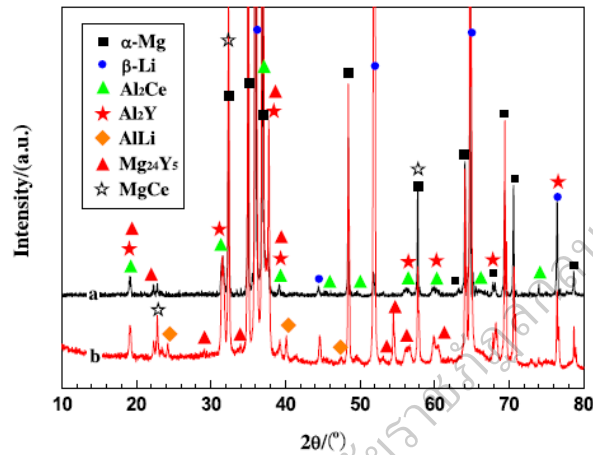

Figure 18 X-ray diffraction (XRD) patterns of Mg-Li-Al-Ce-Y (a) and Mg-Li-Al-Ce-Y-Zn (b) alloys
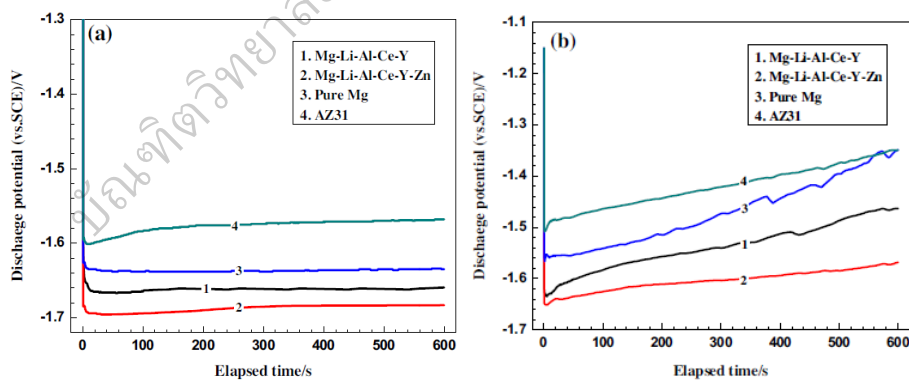(Naiguang Wang, 2016)

Figure 19 Galvanostatic potential-time curves of pure magnesium, AZ31, Mg-Li-Al-Ce-Y, and Mg-Li-Al-Ce-Y-Zn alloys in 3.5 wt.% NaCl solution at 10 mA•cm^{-2} (a) and 180 mA•cm^{-2} (b)
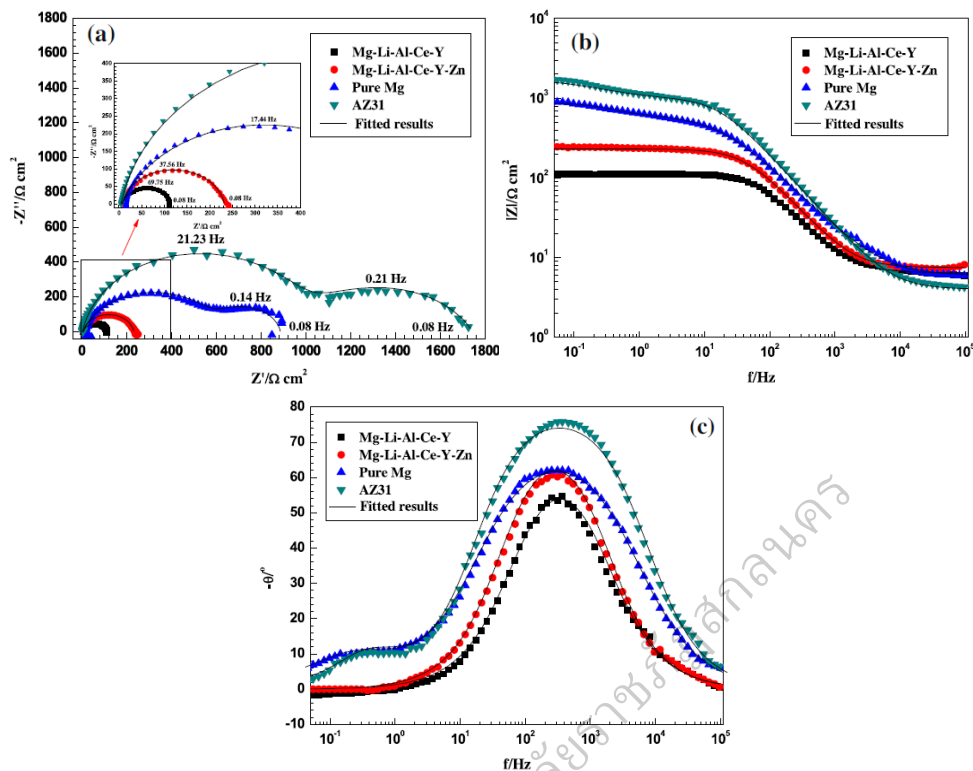(Naiguang Wang, 2016)

Figure 20 Electrochemical impedance spectra (EIS) of pure magnesium, AZ31, Mg-Li-Al-Ce-Y, and Mg-Li-Al-Ce-Y-Zn alloys in 3.5 wt.% NaCl solution: (a) Nyquist plots, (b) Bode plots of impedance modulus vs. frequency, and (c) Bode plots of phase anglevs. frequency
(Naiguang Wang, 2016)

In 2017, A.V. Ilyukhina et al. reported aluminum-air power sources are receiving increased attention for applications in portable electronic devices, transportation, and energy systems. This study reports on the development of an aluminum-air electrochemical generator (AA ECG) and provides a technical foundation for the selection of its components, i.e., aluminum anode, gas diffusion cathode, and alkaline electrolyte. A prototype 1.5 kW AA ECG with specific energy of 270 Wh•kg^{-1} is built and tested. The results of this study demonstrate the feasibility of AA ECGs as portable reserve and emergency power sources, as well as power sources for electric vehicles.
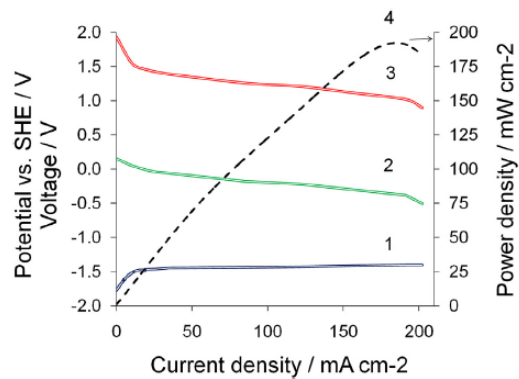
Figure 21 Galvanodynamic polarization curves of the anode (1) and the cathode (2), current-voltage curve (3), and power curve (4) of AA cell with 8 mol NaOH þ 0.015 mol $Na_2SnO_3 \cdot 3H_2O$ at 60 °C
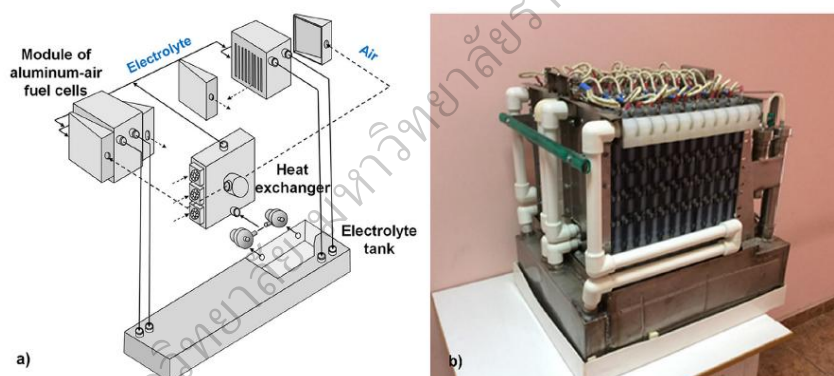(A.V. Ilyukhina, 2017)

Figure 22 Schematic (a) and photograph (b) of AA ECG
(A.V. Ilyukhina, 2017)

In 2017, Harish Medhashree et al. reported the automobiles use magnesium alloys in the components of the enginecoolant systems. These engine coolants used are mainly composed of aqueous ethyleneglycol along with some inhibitors. Generally the engine coolants are contaminated by environmental anions like chlorides, which would enhance the rate of corrosion of the alloysused in the coolant system. In the present study, the corrosion behavior of Mg–Al–Zn–Mn alloy in 30% (v/v) aqueous ethylene glycol containing chloride anions at neutral pH is investigated. Electrochemical techniques, such as

potentiodynamic polarization method, cyclic polarization and electrochemical impedance spectroscopy (EIS) are used to study the corrosion behavior of Mg–Al–Zn–Mn alloy. The surface morphology, microstructure and surface composition of the alloy are studied by using the scanning electron microscopy (SEM), optical microscopy and energy dispersion X-ray (EDX) analysis, respectively. Electrochemical investigations show that the rate of corrosion increases with the increase in chloride ion concentration and also with the increase in medium temperature .
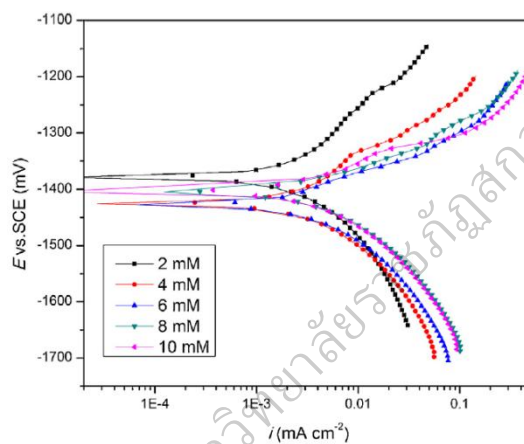

Figure 23 Potentiodynamic polarization plots for the corrosionof Mg–Al–Zn–Mn alloy in 30% aqueous ethylene glycolcontaining different concentrations of the chloride ions at 50 °C

(Harish Medhashree, 2017)

Table 4 Activation parameters for the corrosion of Mg–Al–Zn–Mn alloy

Concentration of Cl⁻ (mM)	E_a (kJ mol⁻¹)	$\Delta H^{\#}$ (kJ mol⁻¹)	$\Delta S^{\#}$ (J mol⁻¹)
2	21.62	19.02	-201.52
4	20.91	18.31	-201.29
6	23.92	21.32	-189.87
8	19.78	17.18	-20248
10	16.12	13.52	-213.15

(Harish Medhashree, 2017)

        In 2017, In-Jun Park et al. reported the effects of Zn and In additions on the aluminum anode for Al-air battery in alkaline solution are examined by the self-corrosion rate, cell voltage, current-voltage characteristics, anodic polarization as shown in Figure 24, discharge performance and AC impedance measurements. The passivation behavior of Zn-added anode during anodic polarization decreases the discharge performance of Al-air battery. The addition of In to Al-Zn anode reduces the formation of Zn passivation film by repeated adsorption and desorption behavior of In ion on to anode surface. The attenuated Zn passive layer by In ion attack leads to the improvement of discharge performance of Al-air battery exhibited in Figure 25.
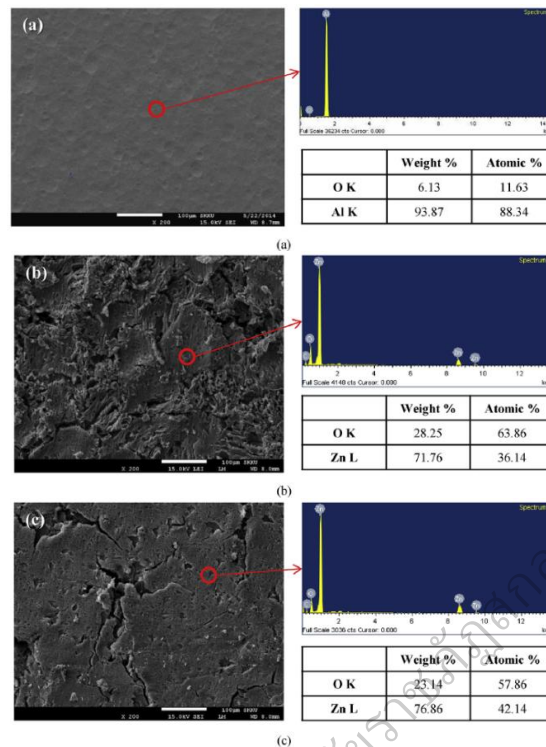
Figure 24 SEM images of anode electrodes after 60 min immersion test in 4 mol
NaOH; (a) 4N Al anode, (b) Al-Zn anode, (c) Al-Zn-In anode
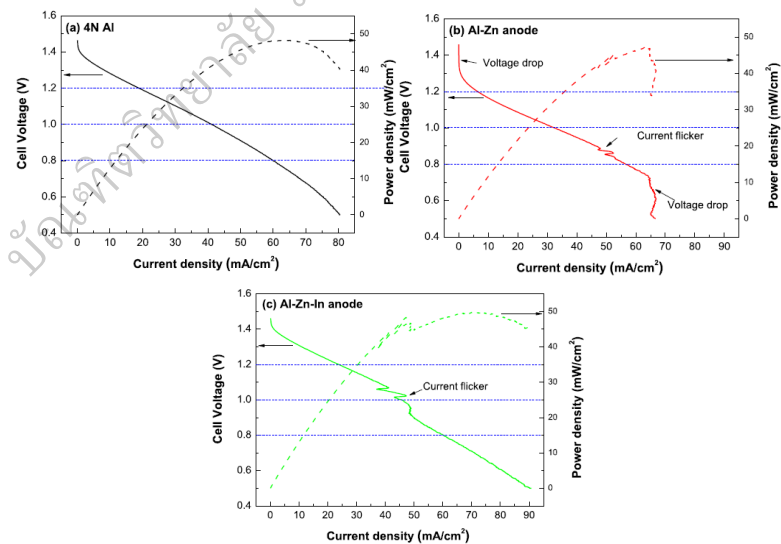(In-Jun Park, 2017)

Figure 25 I-V and I-P curves of three anodes for the full-cell in 4 mol NaOH;
(a) 4N Al, (b) Al-Zn, (c) Al-Zn-In
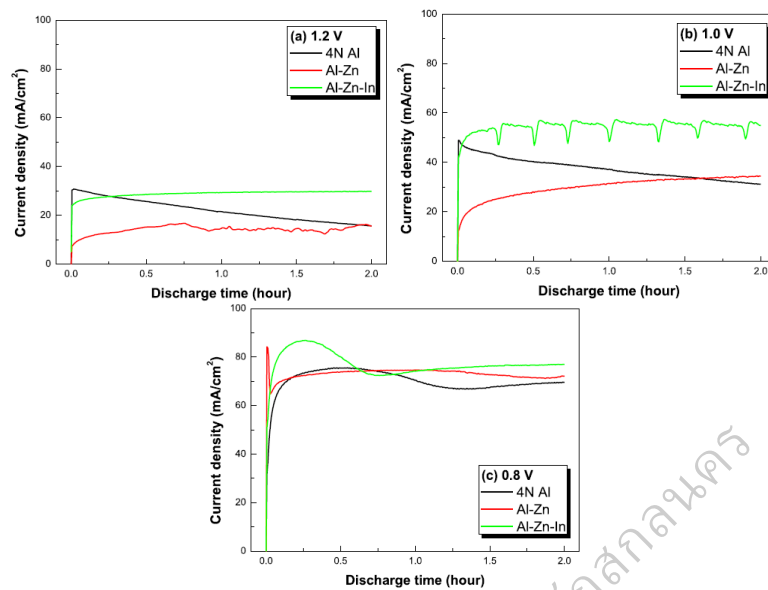(In-Jun Park, 2017)

Figure 26 Discharge behavior of anodes at different discharge voltages;
(a) 1.2 V, (b) 1.0 V, (c) 0.8 V
(In-Jun Park, 2017)

In 2017, Jiarun Li et al. investigated the microstructures and discharge products of Mg-6%Al-3%Zn and Mg-6%Al-3%Zn-0.5% In alloys by morphology observation, phase characterization, and composition analysis as shown in Figure 27. Hydrogen collection, weight-loss measurement, and electrochemical tests are conducted to discuss their corrosion and discharge behaviors. An indium aroused dissolution–reprecipitation mechanism for Mg activation is proposed. Results suggest that the dissolution–reprecipitation mechanism can suitably interpret the indium-activation effect. Indium addition into Mg promotes Mg dissolution through synergistic effects, which involve increasing the second-phase amount, generating less-protective products, promoting products self-peeling, and dissolution–reprecipitation of indium as give in Figure 28. The homogenized Mg-Al-Zn-In alloy performs desirable corrosion resistance and discharge capability and thus is a promising candidate for applications as anode materials.
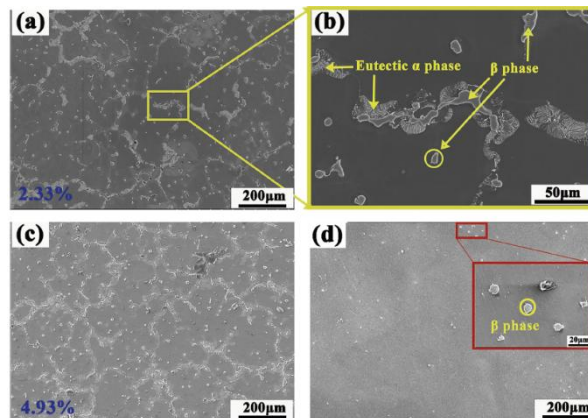
Figure 27 SEM images of investigated alloys: (a) AZ63 alloy; (b) details of the
microstructure framed in (a); (c) AZI alloy; and (d) AZIT alloy and its partial
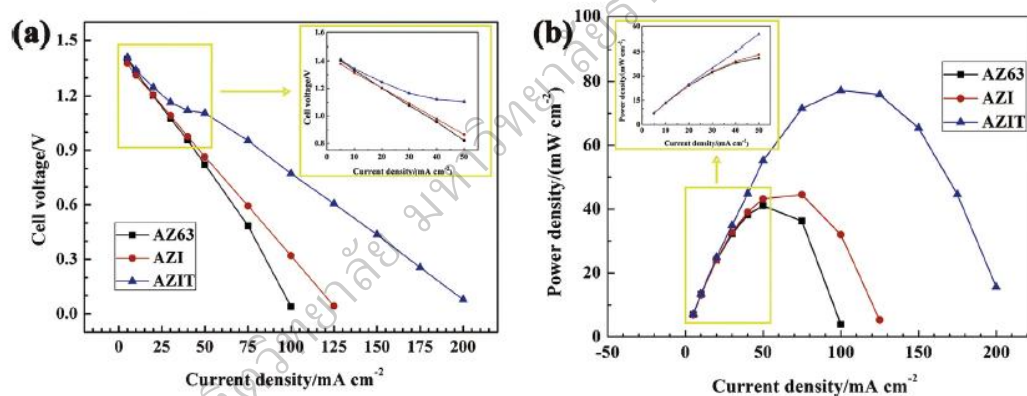enlargement
(Jiarun Li, 2017)

Figure 28 Performance of Mg-CuCl seawater-activated cell with AZ63, AZI and
AZIT anodes in 3.5 wt.%NaCl at ambient temperature: Plots of current
density vs. cell voltage (a) and plots of current density vs.
power density (b)
(Jiarun Li, 2017)

In 2017, M.J. Hutchison et al. evaluated corrosion commercially pure
Cu (Cu), Cu-4.5Sn-0.1Zn, and Cu-9.7Sn-0.1Zn (wt%) and cation release in modified
artificial human perspiration solution. Open circuit corrosion exposures are
conducted for up to 130 hours to determine corrosion rate and the fate of Cu
and Sn. Released aqueous ionconcentrations monitored via inductively-coupled

plasma-optical emission spectroscopy (ICP-OES). Operando atomic emission spectroelectrochemistry (AESEC) analysis is utilized to elucidate thefate of Cu, whether in oxides or solution and deduce the dominant valence states, Cu(I)/Cu(II), of soluble Cu in artificial perspiration. Sn is not observed as a soluble ionic species within ICP-OES or AESEC limitsof detection (LOD). Corrosion products were characterized using grazing incidence X-ray diffraction (GIXRD), Raman spectroscopy, and X-ray photo electron spectroscopy (XPS), and quantified with coulometric reduction (CR). Cu-4.5Sn-0.1Zn displayed the highest corrosion rates in artificial perspiration, followed by Cu-9.7Sn-0.1Zn, and then Cu. Primary corrosion products were Cu_2O, withCuCl as an outer solid product, and an inner layer of SnO_2 for Sn-containing alloys. Cu was dissolved ascuprous (Cu^+) ions. Minor Sn alloying in solid solution catalyzed Cu dissolution which is counteracted at higher Sn contents by a passivating layer of SnO_2, achieving complete passivity at 10.3 wt% Sn according to graph theory. Cu-9.7Sn-0.1Zn indicated semi-passive behavior, speculated to be due a SnO_2 layer and close proximity (9.7 wt%) to this critical value for passivation (10.3 wt%). The effect of alloyed Sn as adissolution promoter for electrochemical Cu ion release, critical Sn contents for passivity, and subsequent implications of antimicrobial function are discussed. Oxidized Zn is not detected above LOD nor demonstrated any measurable effect on corrosion in artificial perspiration.
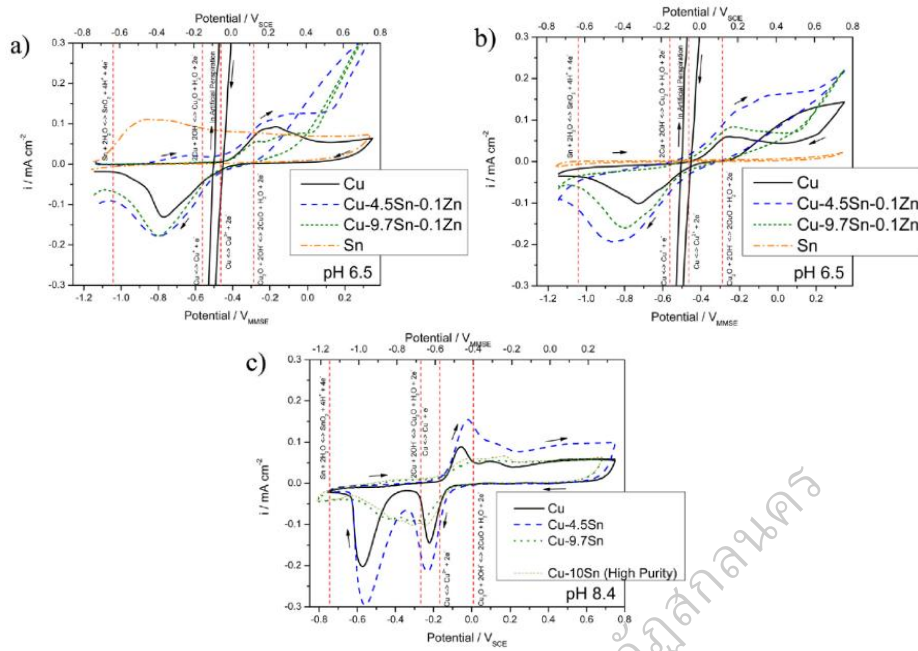
Figure 29 Cyclic voltammograms in deaerated boric acid buffer (pH 6.5) and boratebuffer (pH 8.4). a) Boric acid buffer cycle 1, b) boric acid buffer cycle 3, c) boratebuffer cycle 3. Scan rate 10 mV/s. Samples were held at1.4 V_{MMSE} for 10 min priorto initial scan
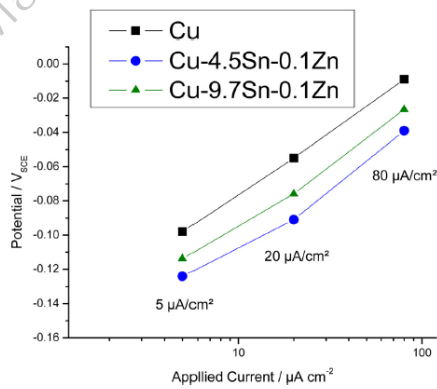(M.J. Hutchison, 2017)

Figure 30 Measured potential plotted against applied current during anodic dissolution stage of AESEC measurements in artificial perspiration
(M.J. Hutchison, 2017)

In 2017, Ran Li et al. fabricated a three-dimensional nanoporous bimetallic Ag-Cu alloy with uniform chemical composition by dealloying $Mg_{65}Ag_{12.5}Cu_{12.5}Y_{10}$ metallic glass in dilute (0.04 M) H_2SO_4 aqueous solution under free-corrosion conditions. The nanoporous Ag-Cu evolves through two distinct stages. First, liga-ments of the nanoporous structure, consisting of supersaturated Ag(Cu) solid solution with a constant Ag/Cu mole ratio of 1:1, are yielded. Second, with excessive immersion, some Cu atoms separate from the metastable nanoporous matrix and form spherical Cu particles on the sample surface. Formation and evolution mechanisms of the nanoporous structure are proposed.
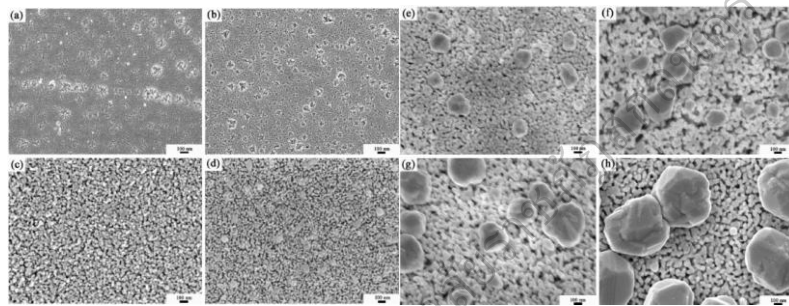

Figure 31 SEM images of the microstructure of nanoporous Ag-Cu derived from dealloyed $Mg_{65}Ag_{12.5}Cu_{12.5}Y_{10}$ metallic glass in 0.04 M H_2SO_4 aqueous solution for different immersion times: (a) 5 min; (b) 10 min; (c) 30 min; (d) 50 min; (e) 60 min; (f) 70 min; (g) 80 min; (h) 90 min
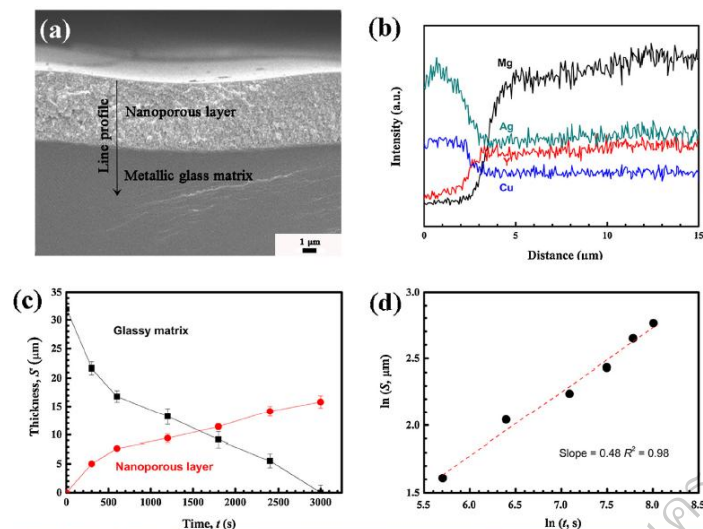
(Ran Li, 2017)

Figure 32 Reaction interface between the corrosion layer and the metallic glass
matrix after dealloying $Mg_{65}Ag_{12.5}Cu_{12.5}Y_{10}$ glassy precursor for 5 min:
(a) cross-section SEMimage and (b) linear composition profile across
the reaction interface. Influence of immersion time (t) on the thicknesses
(T) of the nanoporous Ag-Cu layer and the glassymatrix in free-corrosion
conditions: plots on (c) normal scale and (d) logarithmic scale for
measurement of the growth exponent (n)
The standard deviation of the measuredthickness is
provided asthe error bar in the plot
(Ran Li, 2017)

I have investigate theoretical of battery and literature review found
that all battery used Lead; Pb and Sulfuric acid; H_2SO_4 which it has been effect to
environment. Therefore, I will be changed the Pb and H_2SO_4 into Cu, Al-Zn and
NaCl solution by prepare Cu anode and Al cathode by hot press method, to
measure characteristic, crystal structure, microstructure, resistance and to
discharge of Cu anode and Al cathode and to study possibility of electrochemical
cells of Cu anode and Al cathode in NaCl+DI water.